ACS Energy LETTERS

http://pubs.acs.org/journal/aelccp

LETTER

Slow Electron–Hole Recombination in Lead Iodide Perovskites Does Not Require a Molecular Dipole

Subham Dastidar,[†] Siming Li,[†] Sergey Y. Smolin, Jason B. Baxter, and Aaron T. Fafarman*

Department of Chemical and Biological Engineering, Drexel University, 3141 Chestnut Street, Philadelphia, Pennsylvania 19104, United States

Supporting Information

ABSTRACT: Hybrid organic/inorganic lead iodide perovskites of the formula $APbI_3$, where A is a molecular cation such as methylammonium, exhibit remarkably slow photoinduced charge carrier recombination rates, for reasons that remain uncertain. Prevalent hypotheses credit this behavior to the unique dipolar nature of the molecular cation. Herein, transient terahertz spectroscopy is applied to solution-processed, all-inorganic, perovskite-phase cesium lead iodide ($CsPbI_3$) thin films, which lack such a dipole. The recombination kinetics are studied as a function of the initial photoinduced carrier concentration and the wavelength of excitation. A kinetic model combining diffusion and recombination is fit to the data, from which the rate constants are determined, revealing a bimolecular recombination rate of 10^{-10} cm^3 s^{-1}, comparable to high-quality, single-crystal, direct-gap semiconductors. This rate, as well as a charge carrier mobility > 30 cm^2 V^{-1} s^{-1} measured herein for $CsPbI_3$, are similar to values reported for the hybrid perovskites, strongly suggesting that the organic cation does not confer a fundamental advantage.

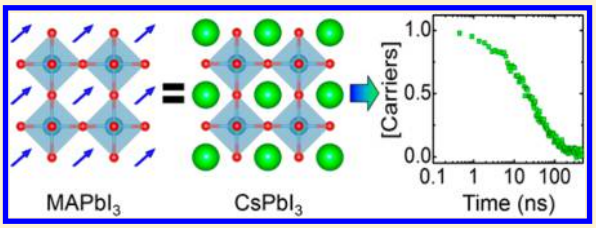

Organic–inorganic hybrid perovskites (OHPs), with the formula ABX_3, are under intense study as possible next-generation photovoltaic absorber materials. Devices made from compositions wherein A is an organic cation such as methylammonium (MA) or formamidinium (FA), B is lead (Pb), and X is iodide have achieved power conversion efficiencies (PCEs) as high as 22%.[1] This performance is strongly determined by the product of the charge carrier mobility (μ) and the excited carrier lifetime (τ), which governs whether photoexcited carriers can be collected in a photovoltaic device.[2] Of particular interest are the extremely high values of τ, which suggest that carrier recombination is atypically slow in these materials.[3−5] However, τ is not a fundamental material parameter; it is instead a function of the conditions of excitation. To highlight the fundamentally anomalous recombination processes and to create an absolute scale to define "slow" recombination, it is sufficient to compare just the bimolecular recombination rate constant to that predicted for two oppositely charged species freely diffusing in a continuous medium. The observed bimolecular recombination rate in hybrid lead halide perovskites is 5 orders of magnitude slower than this so-called Langevin limit.[3,6] Attempts to understand the origins of these extraordinary recombination kinetics often evoke the unique effects of the molecular dipole within the crystal structure.[4,7−11] Interestingly, in this regard, the partial replacement of a fraction of A-site cations with cesium to form "mixed cation" perovskites maintains the excellent charge carrier dynamics observed when the A-site is purely organic.[12−16] Here, we investigate the impact of the complete replacement of the A-site with cesium, yielding an all-inorganic $CsPbI_3$ perovskite, on the excited charge carrier lifetime and mobility.

It is already known that $CsPbX_3$ (X = Br^-, I^-) perovskites have only slightly larger band gaps ($E_{g,Br}$ = 2.36 eV;[17] $E_{g,I}$ = 1.73 eV[18,19]) in comparison to those of methylammonium lead halide ($MAPbX_3$) and a similarly high absorption coefficient[20] and small exciton binding energy.[21,22] $CsPbX_3$ perovskites have very recently found uses in laser,[23−25] light-emitting diode,[26,27] photon detector,[28−30] and photovoltaic[17,31−35] applications. $CsPbBr_3$ has demonstrated slightly lower photovoltaic performance compared to its hybrid counterpart, $MAPbBr_3$,[17] however with enhanced thermal stability.[13,36] More fundamentally, reports differ on whether single-crystal $CsPbBr_3$ has 3-fold[37] or 2 orders-of-magnitude lower[30] values of $\mu\cdot\tau$ compared to $MAPbBr_3$. Even less is currently known about the effect of A-site substitution for the lead iodide perovskites. While $CsPbI_3$ photovoltaics have climbed from an initial ∼3% demonstrated PCE[31] to approximately 10%,[33−35] this value is only half of that of its organic counterpart.

Received: July 10, 2017
Accepted: September 1, 2017
Published: September 1, 2017

DOI: 10.1021/acsenergylett.7b00606
ACS Energy Lett. 2017, 2, 2239−2244

Herein, it is shown that solution-processed $CsPbI_3$ exhibits strikingly similar recombination kinetics and carrier mobility to literature reports of solution-processed $MAPbI_3$. The charge carrier mobility and recombination kinetics of polycrystalline thin films of perovskite-phase $CsPbI_3$ were investigated by pump−probe time-resolved terahertz spectroscopy (TRTS). To understand the contribution of carrier diffusion to the observed kinetics, pump wavelengths of 400, 530, and 650 nm were employed, each creating a different carrier concentration profile throughout the depth of the film. A kinetic model was fit to the transient data to reveal rate constants for the mono-, bi-, and trimolecular recombination processes, parameters typically associated with trap/surface-assisted, radiative, and Auger recombination, respectively. As has been shown with the hybrid perovskites, knowledge of both the rate constants and mobility enables two important calculations: the diffusion length of carriers at fluxes relevant for solar cell operation and the comparison of the bimolecular rate constant to the Langevin limit.[38]

The $CsPbI_3$ thin films were prepared following methods from the literature with modifications. An equimolar warm solution of cesium iodide (CsI) and lead iodide (PbI_2) in dimethylformamide (DMF) was spin-coated on a preheated quartz substrate, initially forming the thermodynamically favored, nonperovskite, yellow δ-$CsPbI_3$ phase.[19,31,39] Subsequent annealing at 350 °C under a N_2 environment transformed the film into the black perovskite phase, or α-$CsPbI_3$. The α-$CsPbI_3$ phase was preserved by rapidly quenching the film to room temperature and maintaining it in a rigorously moisture-free environment[40] for all subsequent measurements.

The transmission spectra for the polycrystalline films, shown in Figure 1, were collected and analyzed with a direct gap Tauc plot (Figure S1a), exhibiting an optical band gap of ∼1.73 eV, in accordance with prior reports.[18,19] The absorption coefficient spectrum is also shown in Figure S1b. SEM images (Figure S2) show the morphology of the film, indicating that the apparent crystal grains are 800 ± 100 nm in size (using the intercept method[41]). The corresponding XRD pattern is shown in Figure S3.

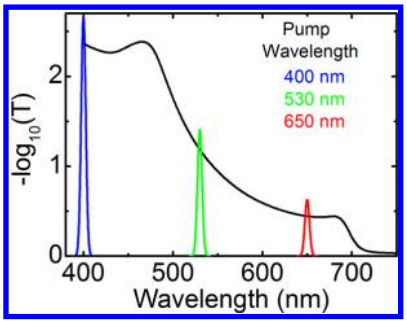

Figure 1. Transmission spectrum of a typical polycrystalline thin film of $CsPbI_3$ used for TRTS measurements, measured in the sample cell, plotted as the logarithm of the transmission. Overlaid are the excitation wavelengths used for TRTS experiments.

TRTS is a noncontact measurement of transient local photoconductivity, capable of reporting on both the relaxation dynamics and the carrier mobility (μ), another critical performance parameter for a solar absorber. TRTS uses an optical pump pulse to photoexcite the sample, followed by a broad-band terahertz-frequency probe pulse at a controlled delay with respect to the pump.[42] The terahertz probe is attenuated in proportion to the photoinduced sheet conductivity, which is in turn proportional to the number of excited carriers per unit area, N, and their mobility, according to $\sigma_{sheet} = \phi \cdot q \cdot N \cdot \sum \mu_i$, where ϕ is the quantum yield of free carriers from absorbed photons, q is the elementary charge and $\sum \mu_i$ is the sum of mobilities of electrons and holes.

Figure 2A−C shows the TRTS signal as a function of time at selected values of the pump power for excitation wavelengths of 400, 530, and 650 nm, respectively. Shorter wavelengths of excitation correspond to higher absorption (see Figure 1 and the Supporting Information for details) and concomitantly steeper gradients in the initial photoexcited carrier density immediately after the pump pulse. For 400 nm excitation, the 240 nm thick film is almost seven times the $1/e$ absorption depth, leading to a significantly higher concentration at the front surface and, consequently, faster recombination, until diffusion acts to reduce the gradient. The 650 nm excitation leads to only a factor of 2 variation in carrier concentration across the whole thickness of the film, minimizing any potential convolution of diffusion with the recombination kinetics. The 530 nm excitation provides an intermediate value that was selected to match the absorptivity of $MAPbI_3$ at 550 nm, in order to facilitate comparison to important literature precedent.[6]

To understand the relative contribution of the different elementary recombination mechanisms, we first identify at which pump fluence values, if any, mono-, bi-, or trimolecular recombination processes dominate. This is achieved by plotting the TRTS signal in functional forms that would be linear for first-, second-, or third-order kinetics, respectively. The results are shown in Figure 2D−F for data taken with 650 nm pump excitation, for which diffusion will have a minimal effect. From a plot of the logarithm of the transient signals versus time, a fluence-independent (first-order recombination-dominated) regime can be identified by straight lines of equal slope at low fluence in Figure 2D (gray curves). At higher fluences, the carrier dynamics are dominated by radiative (second-order, Figure 2E) recombination as these transients all have approximately the same slope when plotted as the inverse of the signal. The contribution from Auger (third-order, Figure 2F) recombination does not dominate at any fluence tested for the 650 excitation. However, the 400 and 530 nm data explore higher carrier concentrations and do exhibit clear third-order kinetics for the highest fluence examples by this analysis (Figure S4). This clear evidence for first-, second-, and third-order processes in $CsPbI_3$ stands in contrast with a transient reflectance study of $CsPbI_2Br$ that was published while the present study was being prepared, in which only first- and third-order processes were in evidence.[43]

To quantify the rate constants for each of the three recombination processes, the TRTS transient data were fit to a diffusion-recombination numerical model using finite-difference techniques. In addition to the three elementary recombination processes modeled in previous studies of halide perovskites,[6] a diffusion term was added, resulting in the following expression

$$\frac{\partial n}{\partial t} = D\frac{\partial^2 n}{\partial x^2} - k_1 n - k_2 n^2 - k_3 n^3 \quad (1)$$

where $n(x,t)$ is the photoexcited charge carrier density at a given time, t, and distance, x, from the illuminated surface of the film. k_1, k_2, and k_3 represent the monomolecular,

DOI: 10.1021/acsenergylett.7b00606
ACS Energy Lett. 2017, 2, 2239−2244

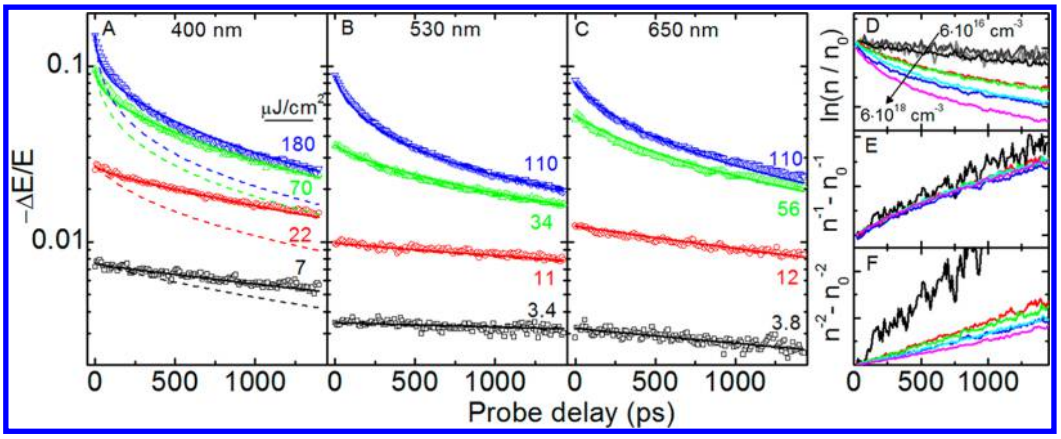

Figure 2. Terahertz transients following an optical pump pulse. (A−C) Transient data are shown as symbols for selected values of the pump fluence (indicated on curve labels). Numerical fits to the data are shown by thin, solid lines. Dashed lines in (A) also show the numerical prediction if diffusion is neglected. Panels (A−C) correspond to 400, 530, and 650 nm pump wavelengths, respectively. (D−F) Transient data for the 650 nm pump wavelength, converted into the estimated average carrier concentration, n, and plotted in functional forms that are linear under pure first-, second-, or third-order kinetics for (D−F), respectively. Transients for all fluence values from 1 to 110 μJ/cm^2 (corresponding to n = 6 to 600 × 10^{16} carriers/cm^3) are shown for panel (D); the two lowest fluence transients are omitted for clarity in panels (E,F).

Table 1. Charge Carrier Recombination Constants for $CsPbI_3$ Compared to Literature Values for $MAPbI_3$ and GaAs

material	monomolecular k_1 (μs^{-1})	bimolecular k_2 ($cm^3\ s^{-1}$)	trimolecular k_3 ($cm^6\ s^{-1}$)	THz mobility $\phi\sum\mu_i$ ($cm^2\ V^{-1}\ s^{-1}$)	comparison to Langevin limit $k_2/(q\cdot\sum\mu_i/\varepsilon_0\varepsilon_r)$
$CsPbI_3$[a]	130 ± 80	(1.9 ± 0.4) × 10^{-10}	(6 ± 4) × 10^{-29}	33 (±5)	2 × 10^{-5}
$MAPbI_{3-x}Cl_x$	–	1.6 × 10^{-10}	4 × 10^{-29}	–	–
$MAPbI_{3-x}Cl_x$ from ref 6	4.9[b]	0.87 × 10^{-10}	9.9 × 10^{-29}	11.6	2.7 × 10^{-5}
intrinsic GaAs from ref 47[b]	–	1.7 × 10^{-10}	0.2 × 10^{-29}	–	–

[a]Error reported as the standard deviation of values from 400, 530, and 650 nm excitation. [b]Determined from time-resolved photoluminescence decay.

bimolecular, and trimolecular recombination rate constants, respectively, and D is the diffusion constant. The initial carrier density profile, $n(x,0)$, is estimated from the pump fluence using Beer's Law and assuming that each absorbed photon creates an electron and hole (i.e., ϕ is assumed to be unity in the equation for photoconductivity above). Under the assumption that the mobility is time-independent, the spectroscopic signal is linearly proportional to the population of photoinduced free carriers. The diffusion constant in the model is a fixed parameter, determined from the measured mobility. The rate constants are globally fit to the complete data sets for each pump wavelength, and the k_i values thus obtained are averaged together (results in Table 1). (For fitting purposes, transients were included from a greater number of fluence values than those shown in Figure 2; complete data are available in Figure S5). Results of the numerical fits are shown in Figure 2A−C as solid lines. To understand the magnitude of the contribution from diffusion, the transients are simulated with the same values of k_i, however with diffusion set to zero, and the results are shown in Figure 2A (dashed lines). For 530 and 650 nm pump wavelengths, the effect of diffusion is minimal. The relatively small differences in the k_2 and k_3 values determined independently for different excitation wavelengths (including one in which the effect of diffusion is significant) and for independently prepared samples enhance confidence in their accuracy compared to measurements employing a single sample or using a single exciting wavelength.

Two interesting points emerge. First, the bimolecular recombination rate for solution-processed $CsPbI_3$ is exceptionally small: it is within a factor of 2 of that reported previously for $MAPbI_{3-x}Cl_x$.[6] To control for any differences in measurement technique or analysis, we performed an independent measurement of $MAPbI_{3-x}Cl_x$, prepared according to literature procedures,[44] on our own optical setup and obtained a value identical to that of $CsPbI_3$ to within our experimental certainty (see Table 1). Quite remarkably, these values for solution-processed materials are similar to those of single-crystal GaAs (Table 1). Second, the monomolecular rate constant, k_1, which is highly sample-dependent (see error bars for this value in Table 1), is nevertheless occasionally quite small, leading to long lifetimes that are comparable to those of $MAPbI_3$. For example, one such champion film showed no measurable decay by TRTS in the 1.5 ns observation window, and therefore, it was studied by transient absorption, using a spectrometer with a ns−μs range (details in the Supporting Information),[45] resulting in a half-life > 20 ns (Figure 3). The dependence of the trap-assisted recombination rate on sample preparation conditions is well-known in the literature on $MAPbI_3$,[46] and increased understanding and optimization of $CsPbI_3$ will likely yield improved control over this variability.

The sum of the electron and hole mobility can be determined from the equation given above for photoconductivity, resulting in a value of 33 cm^2/(V s), assuming ϕ = 1. The value for $CsPbI_3$ is nearly identical to that measured for $MAPbI_3$, using the same technique.[48,49]

DOI: 10.1021/acsenergylett.7b00606
ACS Energy Lett. 2017, 2, 2239−2244

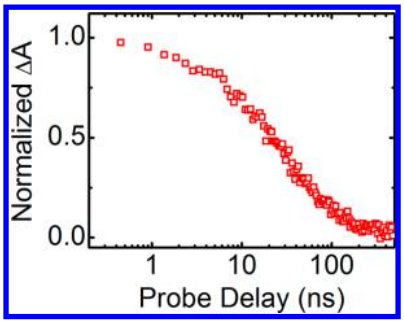

Figure 3. Transient absorption dynamics of the band edge bleach feature for $CsPbI_3$ at a 1.0 $\mu J/cm^2$ pump fluence under 650 nm excitation.

With knowledge of the recombination rate constants and carrier mobilities, we can compare the bimolecular rate constant to the ion capture rate known as the Langevin limit, defined by $\gamma = q\cdot[\sum \mu_i](\varepsilon_r\cdot\varepsilon_0)^{-1}$, where ε_r and ε_0 are the relative and vacuum permittivities, respectively.[50] In the absence of an experimental value for the relative permittivity of $CsPbI_3$ at low frequencies, we use the value of 6 from theoretical calculations[51] as a rough estimate, noting that experimental values of 6.5 are reported in $MAPbI_3$.[52] The Langevin expression provides the rate at which two freely diffusing, oppositely charged carriers in a continuous medium will recombine due to their mutual electrostatic attraction overcoming thermal diffusion. Thus, it provides a rough estimate of the expected rate of bimolecular (electron−hole) recombination for direct-band-gap, low-mobility materials in the absence of any specific screening mechanism beyond simple polarization of the dielectric medium.[50] The measured rate constant is more than 5 orders of magnitude smaller than the Langevin limit, directly indicating that bimolecular recombination is significantly retarded in $CsPbI_3$. Quite importantly, this slowing of recombination is nearly identical to that seen in the hybrid $MAPbI_3$, despite the lack of a molecular dipole. Similar values for the mobility and recombination rate constants are observed for vapor-deposited $MAPbX_3$.[3,38] For reference, the bimolecular recombination rate for $CsPbI_3$ is also compared to that of single-crystal GaAs in Table 1, demonstrating that the solution-processed perovskite is nearly identical in this regard.

To demonstrate the impact of lifetime and mobility on device characteristics, we consider diffusion length, a critical parameter that governs the collection probability of the photogenerated minority carriers in a photovoltaic absorber layer. The diffusion length can be estimated according to $L_D = \sqrt{\mu\tau k_B T/q}$, where τ is the estimated lifetime at carrier densities generated under typical solar illumination, k_B is the Boltzmann constant, and T is temperature. In this low-fluence regime, τ is dominated by monomolecular processes and has the value >20 ns for champion films at a carrier density of 10^{17} cm^{-3}. If we assume approximately balanced electron and hole transport in $CsPbI_3$, as has been observed in $MAPbI_3$,[53] we estimate a single carrier mobility of approximately 16 $cm^2/(V\,s)$. Under these conditions, the estimated diffusion length for $CsPbI_3$ is approximately 1 μm. However, TRTS is a local probe of intragrain transport. Real devices may exhibit somewhat shorter diffusion length owing to lower long-range carrier mobility upon scattering at grain boundaries.[54]

The carrier lifetimes and mobilities measured here are quite similar to those of the hybrid perovskites. However, the susceptibility of the hybrid materials to degradation, principally mediated by their organic component,[55−60] has spurred efforts to develop all-inorganic alternatives. The observation herein of similar performance metrics for $CsPbI_3$ in conjunction with recent progress in enhancing the stability of its perovskite phase,[31,33,61,62] which is not the equilibrium phase at room temperature,[19] suggest great potential for $CsPbI_3$-based photovoltaics. The observation of extremely slow recombination in these materials further calls into question theories that attribute the extraordinary behavior of the hybrid lead halide perovskites to the unique properties of the molecular dipole. In light of the present results, alternative theories such as the direct−indirect band gap structure[63] of lead halide perovskites or a Rashba effect driven by displacive freedom of the A-site atom[64] perhaps deserve greater attention.

■ ASSOCIATED CONTENT

Supporting Information

The Supporting Information is available free of charge on the ACS Publications website at DOI: 10.1021/acsenergylett.7b00606.

Detailed experimental procedures, kinetic modeling, method for diffusion length calculation, material characterization figures, fluence-dependent TRTS plots for $CsPbI_3$ and $MAPbI_{3-x}Cl_x$ (PDF)

■ AUTHOR INFORMATION

Corresponding Author

*E-mail: fafarman@drexel.edu.

ORCID

Subham Dastidar: 0000-0002-3025-4787

Jason B. Baxter: 0000-0001-8702-3915

Author Contributions

†S.D. and S.L. contributed equally to this work.

Notes

The authors declare no competing financial interest.

■ ACKNOWLEDGMENTS

S.D. and A.T.F. acknowledge funding from NSF CBET-1604293. S.L., S.Y.S., and J.B.B. acknowledge funding from NSF DMR-1507988. The ns−μs TA experiments were performed at the Advanced Optical Spectroscopy and Microscopy Facility in the Center for Functional Nanomaterials at Brookhaven National Laboratory. We thank Andrew D. Dillon for helping with the XRD measurement. We are thankful to Swarnendu Chatterjee for collecting the SEM images.

■ REFERENCES

(1) Saliba, M.; Matsui, T.; Domanski, K.; Seo, J.-Y.; Ummadisingu, A.; Zakeeruddin, S. M.; Correa-Baena, J.-P.; Tress, W. R.; Abate, A.; Hagfeldt, A.; et al. Incorporation of Rubidium Cations into Perovskite Solar Cells Improves Photovoltaic Performance. *Science* **2016**, *354*, 206−209.

(2) Stranks, S. D.; Eperon, G. E.; Grancini, G.; Menelaou, C.; Alcocer, M. J. P.; Leijtens, T.; Herz, L. M.; Petrozza, A.; Snaith, H. J. Electron-Hole Diffusion Lengths Exceeding 1 Micrometer in an Organometal Trihalide Perovskite Absorber. *Science* **2013**, *342*, 341−344.

(3) Johnston, M. B.; Herz, L. M. Hybrid Perovskites for Photovoltaics: Charge-Carrier Recombination, Diffusion, and Radiative Efficiencies. *Acc. Chem. Res.* **2016**, *49*, 146−154.

(4) Chen, Y.; Yi, H. T.; Wu, X.; Haroldson, R.; Gartstein, Y. N.; Rodionov, Y. I.; Tikhonov, K. S.; Zakhidov, A.; Zhu, X.-Y.; Podzorov,

DOI: 10.1021/acsenergylett.7b00606
ACS Energy Lett. 2017, 2, 2239−2244

V. Extended Carrier Lifetimes and Diffusion in Hybrid Perovskites Revealed by Hall Effect and Photoconductivity Measurements. *Nat. Commun.* **2016**, *7*, 12253.
(5) Semonin, O. E.; Elbaz, G. A.; Straus, D. B.; Hull, T. D.; Paley, D. W.; van der Zande, A. M.; Hone, J. C.; Kymissis, I.; Kagan, C. R.; Roy, X.; et al. Limits of Carrier Diffusion in N-Type and p-Type $CH_3NH_3PbI_3$ Perovskite Single Crystals. *J. Phys. Chem. Lett.* **2016**, *7*, 3510−3518.
(6) Wehrenfennig, C.; Eperon, G. E.; Johnston, M. B.; Snaith, H. J.; Herz, L. M. High Charge Carrier Mobilities and Lifetimes in Organolead Trihalide Perovskites. *Adv. Mater.* **2014**, *26*, 1584−1589.
(7) Frost, J. M.; Butler, K. T.; Brivio, F.; Hendon, C. H.; van Schilfgaarde, M.; Walsh, A. Atomistic Origins of High-Performance in Hybrid Halide Perovskite Solar Cells. *Nano Lett.* **2014**, *14*, 2584−2590.
(8) Jankowska, J.; Prezhdo, O. V. Ferroelectric Alignment of Organic Cations Inhibits Nonradiative Electron−Hole Recombination in Hybrid Perovskites: Ab Initio Nonadiabatic Molecular Dynamics. *J. Phys. Chem. Lett.* **2017**, *8*, 812−818.
(9) Zhu, X.-Y.; Podzorov, V. Charge Carriers in Hybrid Organic−Inorganic Lead Halide Perovskites Might Be Protected as Large Polarons. *J. Phys. Chem. Lett.* **2015**, *6*, 4758−4761.
(10) Ma, J.; Wang, L.-W. Nanoscale Charge Localization Induced by Random Orientations of Organic Molecules in Hybrid Perovskite $CH_3NH_3PbI_3$. *Nano Lett.* **2015**, *15*, 248−253.
(11) Motta, C.; El-Mellouhi, F.; Kais, S.; Tabet, N.; Alharbi, F.; Sanvito, S. Revealing the Role of Organic Cations in Hybrid Halide Perovskite $CH_3NH_3PbI_3$. *Nat. Commun.* **2015**, *6*, 7026.
(12) Lee, J.-W.; Kim, D.-H.; Kim, H.-S.; Seo, S.-W.; Cho, S. M.; Park, N.-G. Formamidinium and Cesium Hybridization for Photo- and Moisture-Stable Perovskite Solar Cell. *Adv. Energy Mater.* **2015**, *5*, 1501310.
(13) Kulbak, M.; Gupta, S.; Kedem, N.; Levine, I.; Bendikov, T.; Hodes, G.; Cahen, D. Cesium Enhances Long-Term Stability of Lead Bromide Perovskite-Based Solar Cells. *J. Phys. Chem. Lett.* **2016**, *7*, 167−172.
(14) Li, W.; Li, J.; Niu, G.; Wang, L. Effect of Cesium Chloride Modification on the Film Morphology and UV-Induced Stability of Planar Perovskite Solar Cells. *J. Mater. Chem. A* **2016**, *4*, 11688−11695.
(15) McMeekin, D. P.; Sadoughi, G.; Rehman, W.; Eperon, G. E.; Saliba, M.; Hörantner, M. T.; Haghighirad, A.; Sakai, N.; Korte, L.; Rech, B.; et al. A Mixed-Cation Lead Mixed-Halide Perovskite Absorber for Tandem Solar Cells. *Science* **2016**, *351*, 151−155.
(16) Li, Z.; Yang, M.; Park, J.-S.; Wei, S.-H.; Berry, J. J.; Zhu, K. Stabilizing Perovskite Structures by Tuning Tolerance Factor: Formation of Formamidinium and Cesium Lead Iodide Solid-State Alloys. *Chem. Mater.* **2016**, *28*, 284−292.
(17) Kulbak, M.; Cahen, D.; Hodes, G. How Important Is the Organic Part of Lead Halide Perovskite Photovoltaic Cells? Efficient CsPbBr3 Cells. *J. Phys. Chem. Lett.* **2015**, *6*, 2452−2456.
(18) Møller, C. K. Crystal Structure and Photoconductivity of Cæsium Plumbohalides. *Nature* **1958**, *182*, 1436−1436.
(19) Trots, D. M.; Myagkota, S. V. High-Temperature Structural Evolution of Caesium and Rubidium Triiodoplumbates. *J. Phys. Chem. Solids* **2008**, *69*, 2520−2526.
(20) De Roo, J.; Ibáñez, M.; Geiregat, P.; Nedelcu, G.; Walravens, W.; Maes, J.; Martins, J. C.; Van Driessche, I.; Kovalenko, M. V.; Hens, Z. Highly Dynamic Ligand Binding and Light Absorption Coefficient of Cesium Lead Bromide Perovskite Nanocrystals. *ACS Nano* **2016**, *10*, 2071−2081.
(21) Protesescu, L.; Yakunin, S.; Bodnarchuk, M. I.; Krieg, F.; Caputo, R.; Hendon, C. H.; Yang, R. X.; Walsh, A.; Kovalenko, M. V. Nanocrystals of Cesium Lead Halide Perovskites ($CsPbX_3$, X = Cl, Br, and I): Novel Optoelectronic Materials Showing Bright Emission with Wide Color Gamut. *Nano Lett.* **2015**, *15*, 3692−3696.
(22) Li, J.; Yuan, X.; Jing, P.; Li, J.; Wei, M.; Hua, J.; Zhao, J.; Tian, L. Temperature-Dependent Photoluminescence of Inorganic Perovskite Nanocrystal Films. *RSC Adv.* **2016**, *6*, 78311−78316.
(23) Yakunin, S.; Protesescu, L.; Krieg, F.; Bodnarchuk, M. I.; Nedelcu, G.; Humer, M.; De Luca, G.; Fiebig, M.; Heiss, W.; Kovalenko, M. V. Low-Threshold Amplified Spontaneous Emission and Lasing from Colloidal Nanocrystals of Caesium Lead Halide Perovskites. *Nat. Commun.* **2015**, *6*, 8056.
(24) Fu, Y.; Zhu, H.; Stoumpos, C. C.; Ding, Q.; Wang, J.; Kanatzidis, M. G.; Zhu, X.; Jin, S. Broad Wavelength Tunable Robust Lasing from Single-Crystal Nanowires of Cesium Lead Halide Perovskites ($CsPbX_3$, X = Cl, Br, I). *ACS Nano* **2016**, *10*, 7963−7972.
(25) Eaton, S. W.; Lai, M.; Gibson, N. A.; Wong, A. B.; Dou, L.; Ma, J.; Wang, L.-W.; Leone, S. R.; Yang, P. Lasing in Robust Cesium Lead Halide Perovskite Nanowires. *Proc. Natl. Acad. Sci. U. S. A.* **2016**, *113*, 1993−1998.
(26) Dursun, I.; Shen, C.; Parida, M. R.; Pan, J.; Sarmah, S. P.; Priante, D.; Alyami, N.; Liu, J.; Saidaminov, M. I.; Alias, M. S.; et al. Perovskite Nanocrystals as a Color Converter for Visible Light Communication. *ACS Photonics* **2016**, *3*, 1150−1156.
(27) Li, G.; Rivarola, F. W. R.; Davis, N. J. L. K.; Bai, S.; Jellicoe, T. C.; de la Peña, F.; Hou, S.; Ducati, C.; Gao, F.; Friend, R. H.; et al. Highly Efficient Perovskite Nanocrystal Light-Emitting Diodes Enabled by a Universal Crosslinking Method. *Adv. Mater.* **2016**, *28*, 3528−3534.
(28) Stoumpos, C. C.; Malliakas, C. D.; Peters, J. A.; Liu, Z.; Sebastian, M.; Im, J.; Chasapis, T. C.; Wibowo, A. C.; Chung, D. Y.; Freeman, A. J.; et al. Crystal Growth of the Perovskite Semiconductor $CsPbBr_3$: A New Material for High-Energy Radiation Detection. *Cryst. Growth Des.* **2013**, *13*, 2722−2727.
(29) Song, J.; Xu, L.; Li, J.; Xue, J.; Dong, Y.; Li, X.; Zeng, H. Monolayer and Few-Layer All-Inorganic Perovskites as a New Family of Two-Dimensional Semiconductors for Printable Optoelectronic Devices. *Adv. Mater.* **2016**, *28*, 4861−4869.
(30) Dirin, D. N.; Cherniukh, I.; Yakunin, S.; Shynkarenko, Y.; Kovalenko, M. V. Solution-Grown $CsPbBr_3$ Perovskite Single Crystals for Photon Detection. *Chem. Mater.* **2016**, *28*, 8470−8474.
(31) Eperon, G. E.; Paternò, G. M.; Sutton, R. J.; Zampetti, A.; Haghighirad, A. A.; Cacialli, F.; Snaith, H. J. Inorganic Caesium Lead Iodide Perovskite Solar Cells. *J. Mater. Chem. A* **2015**, *3*, 19688−19695.
(32) Ripolles, T. S.; Nishinaka, K.; Ogomi, Y.; Miyata, Y.; Hayase, S. Efficiency Enhancement by Changing Perovskite Crystal Phase and Adding a Charge Extraction Interlayer in Organic Amine Free-Perovskite Solar Cells Based on Cesium. *Sol. Energy Mater. Sol. Cells* **2016**, *144*, 532−536.
(33) Swarnkar, A.; Marshall, A. R.; Sanehira, E. M.; Chernomordik, B. D.; Moore, D. T.; Christians, J. A.; Chakrabarti, T.; Luther, J. M. Quantum Dot-Induced Phase Stabilization of α-$CsPbI_3$ Perovskite for High-Efficiency Photovoltaics. *Science* **2016**, *354*, 92−95.
(34) Frolova, L. A.; Anokhin, D. V.; Piryazev, A. A.; Luchkin, S. Y.; Dremova, N. N.; Stevenson, K. J.; Troshin, P. A. Highly Efficient All-Inorganic Planar Heterojunction Perovskite Solar Cells Produced by Thermal Coevaporation of CsI and PbI_2. *J. Phys. Chem. Lett.* **2017**, *8*, 67−72.
(35) Chen, C.-Y.; Lin, H.-Y.; Chiang, K.-M.; Tsai, W.-L.; Huang, Y.-C.; Tsao, C.-S.; Lin, H.-W. All-Vacuum-Deposited Stoichiometrically Balanced Inorganic Cesium Lead Halide Perovskite Solar Cells with Stabilized Efficiency Exceeding 11%. *Adv. Mater.* **2017**, *29*, 1605290.
(36) Akbulatov, A. F.; Luchkin, S. Y.; Frolova, L. A.; Dremova, N. N.; Gerasimov, K. L.; Zhidkov, I. S.; Anokhin, D. V.; Kurmaev, E. Z.; Stevenson, K. J.; Troshin, P. A. Probing the Intrinsic Thermal and Photochemical Stability of Hybrid and Inorganic Lead Halide Perovskites. *J. Phys. Chem. Lett.* **2017**, *8*, 1211−1218.
(37) Elbaz, G. A.; Straus, D. B.; Semonin, O. E.; Hull, T. D.; Paley, D. W.; Kim, P.; Owen, J. S.; Kagan, C. R.; Roy, X. Unbalanced Hole and Electron Diffusion in Lead Bromide Perovskites. *Nano Lett.* **2017**, *17*, 1727−1732.
(38) Wehrenfennig, C.; Liu, M.; Snaith, H. J.; Johnston, M. B.; Herz, L. M. Charge-Carrier Dynamics in Vapour-Deposited Films of the Organolead Halide Perovskite $CH_3NH_3PbI_{3-x}Cl_x$. *Energy Environ. Sci.* **2014**, *7*, 2269−2275.

DOI: 10.1021/acsenergylett.7b00606
ACS Energy Lett. 2017, 2, 2239−2244

(39) Stoumpos, C. C.; Malliakas, C. D.; Kanatzidis, M. G. Semiconducting Tin and Lead Iodide Perovskites with Organic Cations: Phase Transitions, High Mobilities, and Near-Infrared Photoluminescent Properties. *Inorg. Chem.* **2013**, *52*, 9019−9038.
(40) Dastidar, S.; Hawley, C. J.; Dillon, A. D.; Gutierrez-Perez, A. D.; Spanier, J. E.; Fafarman, A. T. Quantitative Phase-Change Thermodynamics and Metastability of Perovskite-Phase Cesium Lead Iodide. *J. Phys. Chem. Lett.* **2017**, *8*, 1278−1282.
(41) Hoffman, J. B.; Schleper, A. L.; Kamat, P. V. Transformation of Sintered $CsPbBr_3$ Nanocrystals to Cubic $CsPbI_3$ and Gradient $CsPbBr_xI_{3-x}$ through Halide Exchange. *J. Am. Chem. Soc.* **2016**, *138*, 8603−8611.
(42) Guglietta, G. W.; Diroll, B. T.; Gaulding, E. A.; Fordham, J. L.; Li, S.; Murray, C. B.; Baxter, J. B. Lifetime, Mobility, and Diffusion of Photoexcited Carriers in Ligand-Exchanged Lead Selenide Nanocrystal Films Measured by Time-Resolved Terahertz Spectroscopy. *ACS Nano* **2015**, *9*, 1820−1828.
(43) Kennedy, C. L.; Hill, A. H.; Massaro, E. S.; Grumstrup, E. M. Ultrafast Excited-State Transport and Decay Dynamics in Cesium Lead Mixed Halide Perovskites. *ACS Energy Lett.* **2017**, *2*, 1501−1506.
(44) Lee, M. M.; Teuscher, J.; Miyasaka, T.; Murakami, T. N.; Snaith, H. J. Efficient Hybrid Solar Cells Based on Meso-Superstructured Organometal Halide Perovskites. *Science* **2012**, *338*, 643−647.
(45) Milleville, C. C.; Pelcher, K. E.; Sfeir, M. Y.; Banerjee, S.; Watson, D. F. Directional Charge Transfer Mediated by Mid-Gap States: A Transient Absorption Spectroscopy Study of CdSe Quantum Dot/β-$Pb_{0.33}V_2O_5$ Heterostructures. *J. Phys. Chem. C* **2016**, *120*, 5221−5232.
(46) Nie, W.; Tsai, H.; Asadpour, R.; Blancon, J.-C.; Neukirch, A. J.; Gupta, G.; Crochet, J. J.; Chhowalla, M.; Tretiak, S.; Alam, M. A.; et al. High-Efficiency Solution-Processed Perovskite Solar Cells with Millimeter-Scale Grains. *Science* **2015**, *347*, 522−525.
(47) Strauss, U.; Rühle, W. W.; Köhler, K. Auger Recombination in Intrinsic GaAs. *Appl. Phys. Lett.* **1993**, *62*, 55−57.
(48) Milot, R. L.; Eperon, G. E.; Snaith, H. J.; Johnston, M. B.; Herz, L. M. Temperature-Dependent Charge-Carrier Dynamics in $CH_3NH_3PbI_3$ Perovskite Thin Films. *Adv. Funct. Mater.* **2015**, *25*, 6218−6227.
(49) Karakus, M.; Jensen, S. A.; D'Angelo, F.; Turchinovich, D.; Bonn, M.; Cánovas, E. Phonon−Electron Scattering Limits Free Charge Mobility in Methylammonium Lead Iodide Perovskites. *J. Phys. Chem. Lett.* **2015**, *6*, 4991−4996.
(50) Kepler, R. G.; Coppage, F. N. Generation and Recombination of Holes and Electrons in Anthracene. *Phys. Rev.* **1966**, *151*, 610−614.
(51) Murtaza, G.; Ahmad, I. First Principle Study of the Structural and Optoelectronic Properties of Cubic Perovskites $CsPbM_3$ (M = Cl, Br, I). *Phys. B* **2011**, *406*, 3222−3229.
(52) Hirasawa, M.; Ishihara, T.; Goto, T.; Uchida, K.; Miura, N. Magnetoabsorption of the Lowest Exciton in Perovskite-Type Compound $(CH_3NH_3)PbI_3$. *Phys. B* **1994**, *201*, 427−430.
(53) Xing, G.; Mathews, N.; Sun, S.; Lim, S. S.; Lam, Y. M.; Grätzel, M.; Mhaisalkar, S.; Sum, T. C. Long-Range Balanced Electron- and Hole-Transport Lengths in Organic-Inorganic $CH_3NH_3PbI_3$. *Science* **2013**, *342*, 344−347.
(54) Hempel, H.; Redinger, A.; Repins, I.; Moisan, C.; Larramona, G.; Dennler, G.; Handwerg, M.; Fischer, S. F.; Eichberger, R.; Unold, T. Intragrain Charge Transport in Kesterite Thin Films—Limits Arising from Carrier Localization. *J. Appl. Phys.* **2016**, *120*, 175302.
(55) Christians, J. A.; Miranda Herrera, P. A.; Kamat, P. V. Transformation of the Excited State and Photovoltaic Efficiency of $CH_3NH_3PbI_3$ Perovskite upon Controlled Exposure to Humidified Air. *J. Am. Chem. Soc.* **2015**, *137*, 1530−1538.
(56) Misra, R. K.; Aharon, S.; Li, B.; Mogilyansky, D.; Visoly-Fisher, I.; Etgar, L.; Katz, E. A. Temperature- and Component-Dependent Degradation of Perovskite Photovoltaic Materials under Concentrated Sunlight. *J. Phys. Chem. Lett.* **2015**, *6*, 326−330.
(57) Yang, J.; Siempelkamp, B. D.; Liu, D.; Kelly, T. L. Investigation of $CH_3NH_3PbI_3$ Degradation Rates and Mechanisms in Controlled Humidity Environments Using in Situ Techniques. *ACS Nano* **2015**, *9*, 1955−1963.
(58) Noh, J. H.; Im, S. H.; Heo, J. H.; Mandal, T. N.; Seok, S. I. Chemical Management for Colorful, Efficient, and Stable Inorganic−Organic Hybrid Nanostructured Solar Cells. *Nano Lett.* **2013**, *13*, 1764−1769.
(59) Cheng, Z.; Lin, J. Layered Organic−inorganic Hybrid Perovskites: Structure, Optical Properties, Film Preparation, Patterning and Templating Engineering. *CrystEngComm* **2010**, *12*, 2646−2662.
(60) Han, Y.; Meyer, S.; Dkhissi, Y.; Weber, K.; Pringle, J. M.; Bach, U.; Spiccia, L.; Cheng, Y.-B. Degradation Observations of Encapsulated Planar $CH_3NH_3PbI_3$ Perovskite Solar Cells at High Temperatures and Humidity. *J. Mater. Chem. A* **2015**, *3*, 8139−8147.
(61) Dastidar, S.; Egger, D. A.; Tan, L. Z.; Cromer, S. B.; Dillon, A. D.; Liu, S.; Kronik, L.; Rappe, A. M.; Fafarman, A. T. High Chloride Doping Levels Stabilize the Perovskite Phase of Cesium Lead Iodide. *Nano Lett.* **2016**, *16*, 3563−3570.
(62) Luo, P.; Xia, W.; Zhou, S.; Sun, L.; Cheng, J.; Xu, C.; Lu, Y. Solvent Engineering for Ambient-Air-Processed, Phase-Stable $CsPbI_3$ in Perovskite Solar Cells. *J. Phys. Chem. Lett.* **2016**, *7*, 3603−3608.
(63) Hutter, E. M.; Gélvez-Rueda, M. C.; Osherov, A.; Bulović, V.; Grozema, F. C.; Stranks, S. D.; Savenije, T. J. Direct-Indirect Character of the Bandgap in Methylammonium Lead Iodide Perovskite. *Nat. Mater.* **2016**, *16*, 115−120.
(64) Isarov, M.; Tan, L. Z.; Bodnarchuk, M. I.; Kovalenko, M. V.; Rappe, A. M.; Lifshitz, E. Rashba Effect in a Single Colloidal $CsPbBr_3$ Perovskite Nanocrystal Detected by Magneto-Optical Measurements. *Nano Lett.* **2017**, *17*, 5020.

DOI: 10.1021/acsenergylett.7b00606
ACS Energy Lett. 2017, 2, 2239−2244